Mon. Not. R. Astron. Soc. **000**, 1–12 (2013) Printed 23 May 2014 (MN LATEX style file v2.2)

Black hole feedback in a multiphase interstellar medium

Martin A. Bourne[1,⋆], Sergei Nayakshin[1] and Alexander Hobbs[2]
[1] *Department of Physics and Astronomy, University of Leicester, Leicester, LE1 7RH, UK*
[2] *Institute for Astronomy, Department of Physics, ETH Zurich, Wolfgang-Pauli-Strasse 16, CH-8093 Zurich, Switzerland*
⋆ *E-mail:* martin.bourne@le.ac.uk

arXiv:1405.5647v1 [astro-ph.GA] 22 May 2014

Received

ABSTRACT
Ultrafast outflows (UFOs) from supermassive black holes (SMBHs) are thought to regulate the growth of SMBHs and host galaxies, resulting in a number of observational correlations. We present high-resolution numerical simulations of the impact of a thermalized UFO on the ambient gas in the inner part of the host galaxy. Our results depend strongly on whether the gas is homogeneous or clumpy. In the former case all of the ambient gas is driven outward rapidly as expected based on commonly used energy budget arguments, while in the latter the flows of mass and energy decouple. Carrying most of the energy, the shocked UFO escapes from the bulge via paths of least resistance, taking with it only the low-density phase of the host. Most of the mass is however in the high-density phase, and is affected by the UFO much less strongly, and may even continue to flow inwards. We suggest that the UFO energy leakage through the pores in the multiphase interstellar medium (ISM) may explain why observed SMBHs are so massive despite their overwhelmingly large energy production rates. The multiphase ISM effects reported here are probably under-resolved in cosmological simulations but may be included in prescriptions for active galactic nuclei feedback in future simulations and in semi-analytical models.

Key words: galaxies: evolution, galaxies: ISM, galaxies: active, methods: numerical

1 INTRODUCTION

Observational correlations between the mass of supermassive black holes (SMBHs) and their host galaxy, such as the $M-\sigma$ relation (Ferrarese & Merritt 2000; Gebhardt et al. 2000; Tremaine et al. 2002) link the evolution of the SMBH and their host bulge. Feedback (e.g., Silk & Rees 1998) , in the form of ultra fast outflows (UFOs), has been invoked to explain and derive the $M-\sigma$ relation from analytical arguments (King 2003, 2005). The model is very attractive due to its simplicity, reliance on common sense physics (Eddington limit, escape velocity and radiation momentum outflow rate arguments), observational analogy to outflows from massive stars (that are also near their Eddington limits), and finally direct observations of UFOs in nearby bright AGN (Pounds et al. 2003; King & Pounds 2003; Tombesi et al. 2010a,b; Pounds & Vaughan 2011).

Assuming a homogeneous gas distribution following a singular isothermal sphere (SIS) potential (e.g., §4.3.3b in Binney & Tremaine, 2008), King (2003) shows that within the inverse Compton (IC) cooling radius, $R_{\rm IC} \sim 500 M_8^{1/2}\sigma_{200}$ kpc (where M_8 is the SMBH mass in units of $10^8\,{\rm M}_\odot$ and σ_{200} is the velocity dispersion in the host, σ in units of 200 km s^{-1}; Zubovas & King (2012b)), the wind shock, which develops when the UFO collides with the interstellar medium (ISM), can cool effectively via IC scattering. Most of the thermalized wind kinetic energy is lost to this radiation, and only the pre-shock ram pressure impacts the ISM. By considering the equation of motion of the swept up ISM shell, King (2003) derived the mass that the SMBH had to attain in order to clear the host galaxy's gas. Beyond the cooling radius, $R_{\rm IC}$, the wind shock cannot cool effectively and retains the wind kinetic energy in the form of thermal energy and the outflow becomes energy driven. This regime is much more effective at clearing a galaxy of gas.

The model of King (2003) assumes the electrons and ions in the shock share a single temperature at all times, initially the shock temperature $T_{\rm sh} \sim 10^{10}$K. However, Faucher-Giguère & Quataert (2012) have shown that, due to the high temperature and low density of the shocked wind, the electron-ion energy equilibration time-scale is long compared with the Compton time-scale. This would imply that the electron temperature is much lower than the ion temperature, i.e. $T_{\rm e} \ll T_{\rm ion}$. Bourne & Nayakshin (2013) point out an observational test to distinguish between outflows with a one-temperature ($1T$; $T_{\rm e} = T_{\rm i}$) or two-temperature ($2T$) structure, and conclude preliminarily that X-ray observations broadly support the findings of Faucher-Giguère & Quataert (2012). This would however lead to significant implications for AGN feedback on host galaxies: most of

the UFO's kinetic energy, carried by the ions, is then conserved rather than radiated away. The cooling radius, $R_{\rm IC}$, becomes negligibly small on the scale of the host galaxy, and the outflow is essentially always in the energy conserving phase. Based on spherically symmetric analytical models (e.g., King 2005), even black holes ~ 100 times below M_σ could clear a galaxy of its gas. It is then not clear (i) how black holes manage to grow so massive, and (ii) why momentum-conserving flows provide such a tight fit to the observed $M-\sigma$ relations (King 2003).

Several recent additional numerical and analytical results however call the spherically symmetric models of AGN feedback into question. In the context of the physically related problem of stellar feedback, Harper-Clark & Murray (2009) modelled the structure of a hot bubble inflated by a cluster of young stars in Carina Nebula, and have shown that the models assuming spherical symmetry do not explain the observational data. At the same time, a model in which the ambient ISM is clumpy accounts for observations much better. Harper-Clark & Murray (2009) build a toy analytical model in which a significant fraction of the energy inside of the hot bubble is lost via advection, e.g., adiabatic expansion energy losses, rather than radiative energy losses (which can be directly observed in X-rays in the case of Carina Nebula, and are much lower than expected in the spherically symmetric models). Physically, the authors argue that the compressed shell of a multiphase ISM has pores through which the hot gas escapes. This deflates the bubble and allows a much better explanation of the bubble size, age and luminosity.

Rogers & Pittard (2013) have recently performed 3D numerical simulations of a supernova exploding inside an inhomogeneous giant molecular cloud, and found results consistent with that of Harper-Clark & Murray (2009): the densest molecular regions turned out to be surprisingly resistant to ablation by the hot gas which was mainly escaping from the region via low density channels.

For the AGN feedback problem that we study here, Wagner et al. (2012) have found very similar results when studying the interaction of an AGN jet with the multiphase ISM. Furthermore, Wagner et al. (2013) studied the interaction of a wide-angle outflow with an inhomogeneous ambient medium, finding again that hot gas mainly streams away through channels between the cold clouds; the latter are impacted by the momentum of the UFO only. These authors also concluded that the opening angle of the UFO at launch appears secondary, since interactions of the UFO with the intervening clouds isotropize the hot bubble, so that result of a jet and an UFO running into the inhomogeneous ISM may actually be much more similar than often assumed.

In an analytical study, Nayakshin (2014, hereafter N14) also argued that most of the UFO energy leaks out of the porous bulge via the low-density voids, and that the cold gas is affected only by the ram pressure. He argued that the densest cold clouds may continue to feed the AGN via the 'chaotic accretion mode' (Hobbs et al. 2011) despite the AGN blowing an energy-driven bubble into the host galaxy, and that the balance between the ram pressure of the UFO on the clouds and cloud self-gravity leads to an $M-\sigma$ correlation very similar in functional form to that of King (2003).

Furthermore, Zubovas & Nayakshin (2014, ZN14 hereafter) presented numerical simulations of AGN feedback impacting elliptical, initially homogeneous ambient gas distributions and showed that the UFO energy escapes via directions of least resistance (along the minor axis of the ellipsoid). They additionally presented a toy analytical model, similar in spirit to that of Harper-Clark & Murray (2009), which showed that the SMBH growth stops when the SMBH reaches a mass of the order of the King (2003) result. In this paper we investigate these ideas further numerically. We set up a hot bubble of shocked UFO gas bounded by either one- or two-phase ambient gas, and then study the resulting interaction. Our multiphase gas is produced by evolving a Gaussian random velocity field as is frequently done in numerical models of star formation inside turbulent molecular clouds (Bate 2009), similar to earlier work by Hobbs et al. (2011).

Our numerical methods and initial conditions differ substantially from that of Wagner et al. (2012, 2013) and ZN14, but results are qualitatively similar. We also find that most of the UFO energy is carried away by hot low density gas escaping the innermost regions of the host via paths of least resistance, which exists in the clumpy ISM in abundance (e.g., McKee & Ostriker 1977). Most of the gaseous mass in our models is in the high-density cold phase of the ISM that occupies a small fraction of the host's volume, and for this reason our host galaxies turn out to be much less vulnerable to AGN feedback than could be thought based on the energy budget arguments alone.

2 SIMULATION SET-UP

2.1 Numerical method

The simulations presented here make use of a modified version of the N-body/hydrodynamical code GADGET-3, an updated version of the code presented in Springel (2005). We implement the SPHS[1] formalism as described in Read et al. (2010) and Read & Hayfield (2012), in order to correctly treat mixing within multiphase gas, together with a second-order Wendland kernel (Wendland 1995; Dehnen & Aly 2012) with 100 neighbours. The SPHS algorithm was developed for the express purpose of capturing instabilities such as Kelvin-Helmholz and Rayleigh-Taylor, and has been demonstrated as robust in many test problems (Read & Hayfield 2012) and full galaxy formation simulations (Hobbs et al. 2013). The simulations are run in a static isothermal potential with the total mass of the potential within radius R following:

$$M_{\rm pot}(R) = \frac{M_{\rm a}}{a} R \, , \qquad (1)$$

where $M_{\rm a} = 5\times10^{10}$ M$_\odot$ and $a = 4$kpc. The potential is softened at small radii in order to avoid divergence in the gravitational force as R tends to zero. The one dimensional velocity dispersion of the potential is $\sigma_{\rm pot} = (GM_{\rm a}/2a)^{1/2} \simeq 164$ km s^{-1}. In all simulations we use an ideal equation of state for the gas, the gas pressure is given by $P = \rho k_{\rm B} T/\mu m_{\rm p}$, where ρ is the gas density, $k_{\rm B}$ is the Boltzmann constant, T is the gas temperature and $\mu = 0.63$ is the mean molecular

[1] Smooth particle hydrodynamics with a high-order dissipations switch.

weight. An optically thin radiative cooling function for gas ionized and heated by a quasar radiation field (assuming a fixed black hole luminosity of $L_{Edd} = 2.5 \times 10^{46}$ erg s^{-1}) as calculated by Sazonov et al. (2005) is used for $T > 10^4$ K. Below 10^4 K, cooling is modelled as in Mashchenko et al. (2008), proceeding through fine structure and metastable lines of C, N, O, Fe, S and Si. For simplicity, we fix metal abundances at solar metallicity. We impose a temperature floor of 100 K.

Gas particles are converted into star particles according to a Jeans instability condition. SPH particles with density above a critical density of

$$\rho_{crit} = \rho_{thresh} + \rho_J \tag{2}$$

are turned into star particles, where $\rho_{thresh} = 10^{-20}$ g cm^{-3} and ρ_J is the local Jeans density given by,

$$\rho_J = \left(\frac{\pi k_B T}{\mu m_p G}\right)^3 (n_{ngb} m_{sph})^{-2} \simeq 1.17 \times 10^{-18} T_4^3 \text{g cm}^{-3} \tag{3}$$

where $T_4 = T/10^4$ K, $n_{ngb} = 100$ is the typical number of neighbours of an sph particle and m_{sph} is the SPH particle mass. The ρ_{thresh} term ensures that only high-density gas is converted into star particles whilst the second term is the local Jeans density and ensures that stars only form in gas that is unstable towards gravitational collapse[2]. Removing high-density gas aids in reducing the computation time by removing particles that would otherwise have prohibitively short time-steps. Each newly formed star particle has the same mass as the original gas particle and only interact with other particles through gravity.

2.2 Initial conditions

Simulation of isolated galaxies by definition does not model gas inflows into galaxies from larger scales, and therefore idealized initial conditions for the ISM of the host must be used. There is a considerable freedom in choosing these initial conditions. In W12 and W13, cold, high-density clumps in hydrostatic equilibrium with the hot, low-density phase are introduced at the beginning of the simulation. The initial velocity of the gas is zero everywhere.

In the current paper, however, since the epoch we are interested is one of a rapid SMBH growth and star formation in the host galaxy, the ambient gas may be in a very dynamical non-equilibrium state, which we model with an imposed turbulent velocity flow. In doing so we are inspired by numerical studies of star formation in molecular clouds (e.g., Bate et al. 2003). In practice, our method for generating two-phase initial conditions is based on earlier work by Hobbs et al. (2011), where the importance of high-density gas clumps for SMBH *feeding rather than feedback* was studied.

[2] Strictly speaking in order to properly follow the collapse of gas one should be able to resolve the local Jeans mass, M_J, i.e. $n_{ngb} m_{sph} < M_J$ (Whitworth 1998). Gas with $T = T_{floor} = 100$ K has $\rho_J \simeq 10^{-24}$ g cm^{-3} leading to some gas having $\rho > \rho_J$ but not being converted into stars and hence we are not resolving the Jeans mass of this gas. However for the purpose of these simulations we are not particular interested in studying star formation in detail and the number of particles for which the above condition is true is negligibly small.

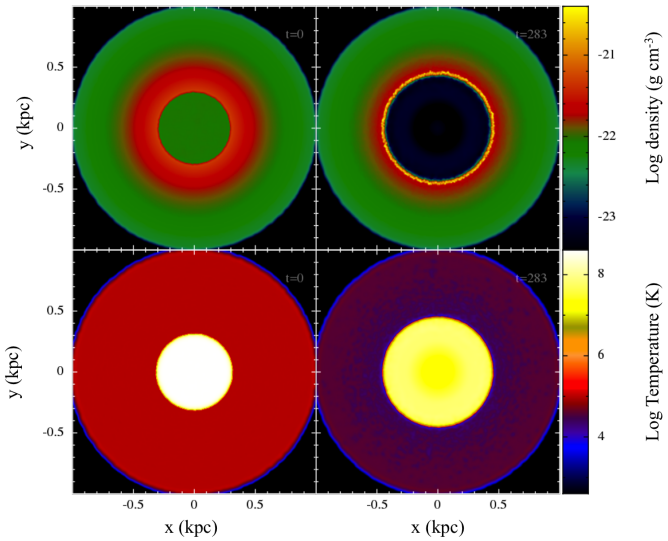

Figure 1. Density (top panel) and temperature (bottom) slices through z=0 plane at time t=0 and $t \simeq 282$ kyr for homogeneous initial condition simulation H1.

We seed a sphere of gas (cut from a relaxed, glass-like configuration) with a turbulent velocity field following Dubinski et al. (1995). A Kolmogorov power spectrum is assumed, $P_v(k) \sim k^{-11/3}$, where k is the wavenumber. Gas velocity $\vec{v}$ can be defined in terms of the vector potential $\vec{A}$, whose realization is also a power-law with the cutoff at $k_{\rm min}$. Physically the small scale cut-off $k_{\rm min}$ defines the largest scale, $\lambda_{\rm max} = 2\pi/k_{\rm min}$, on which turbulence is likely to be driven. Here we set $k_{\rm min} \simeq 1/R_{\rm out}$, as the shell becomes distorted for larger $\lambda_{\rm max}$. The statistical realization of the velocity field is generated by sampling the vector potential $\vec{A}$ in Fourier space, drawing the amplitudes of the components of $\vec{A_{\rm k}}$ at each point (k_x, k_y, k_z) from a Rayleigh distribution with a variance given by $< |\vec{A_{\rm k}}|^2 >$ and assigning phase angles that are uniformly distributed between 0 and 2π. Finally, we take the Fourier transform of $\vec{v_{\rm k}} = i\vec{k} \times \vec{A_{\rm k}}$ to obtain the velocity field in real space.

The gas initially follows the SIS potential (meaning that $\rho(R) \propto R^{-2}$) from $R_{\rm in} = 0.1$ kpc to $R_{\rm out} = 1$ kpc with a gas mass fraction $f_{\rm g} = M_{\rm g}/(M_{\rm g} + M_{\rm pot}) = 0.5$, where $M_{\rm g}$ and $M_{\rm pot}$ are the gas and potential mass within the shell $0.1 \leqslant R \leqslant 1$ kpc, respectively. In order to avoid particles at small radii with prohibitively small time steps we add a sink particle at the centre of the simulation domain with $M_{\rm sink} = 2 \times 10^8\,{\rm M}_\odot$ ($\sim M_\sigma/2$). The turbulent velocity is normalized such that the root-mean-square velocity, $v_{\rm turb} \simeq \sigma \simeq 232$ km s^{-1}, where $\sigma \simeq (GM_{\rm a}/2a(1-f_{\rm g}))^{1/2}$ is the velocity dispersion of the potential plus gas component.

The initial gas temperature is set to $T \simeq 1 \times 10^6$ K, such that the shell is marginally virialized, i.e; $(E_{\rm turb} + E_{\rm therm})/|E_{\rm grav}| \sim 1/2$, where $E_{\rm turb}$ and $E_{\rm therm}$ are the total turbulent kinetic energy and total thermal energy of the gas respectively and $E_{\rm grav}$ is the gravitational potential energy of the system.

The system is allowed to evolve under the action of the turbulent velocity field for time $\sim \tau_{\rm dyn}/3 = R_{\rm out}/3\sigma$,

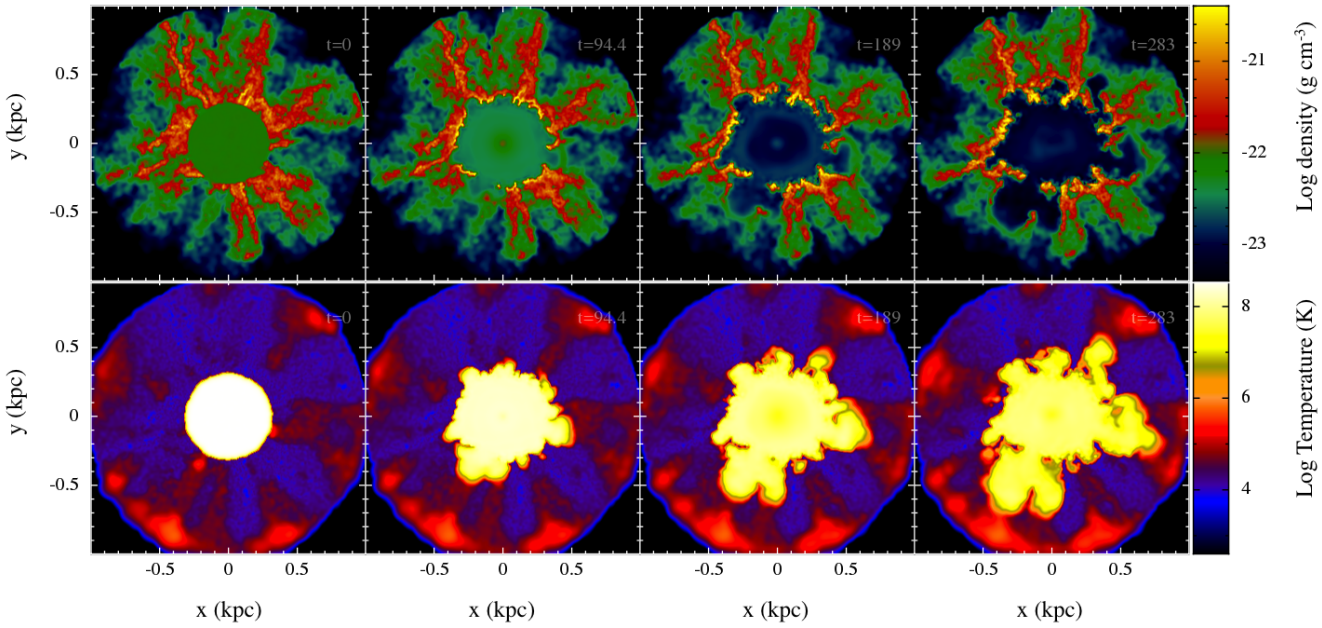

Figure 2. Same as Fig. 1 but for the turbulent initial condition simulation T1. Density (top panel) and temperature (bottom panel) slices through z=0 plane evolving in time from t=0 to $t \simeq 282$ kyr in steps of ~ 94 kyr, from left to right, respectively.

allowing the density inhomogeneities to grow. The resulting gas shell is then re-cut to have an inner radius $R_{\rm in} = 0.3$ kpc and outer radius $R_{\rm out} = 1$ kpc. The total gas mass is $M_{\rm g} \simeq 5.9 \times 10^9\,{\rm M}_\odot$, corresponding to a gas fraction of $f_{\rm g} \simeq 0.4$ and giving a velocity dispersion for the system (gas + potential within the shell) of $\sigma \simeq 212$ kms^{-1}. The total number of particles in the gas shell is $N_{\rm gas} \simeq 2.6 \times 10^6$ with a particle mass $m_{\rm gas} \simeq 2250\,{\rm M}_\odot$.

Typical parameters for an UFO give a velocity $v_{\rm out} \sim 0.1$ c, mass outflow rate $\dot{M}_{\rm out} \sim 0.1\,{\rm M}_\odot$ yr^{-1} and kinetic energy flux $\dot{M}_{\rm out}v^2/2 \simeq 0.05 L_{\rm Edd}$. Modelling a continuous ejection of fast wind particles by SPH is not currently feasible: at our present mass resolution (which is much higher than a typical cosmological simulation), a single SPH particle accounts for all of the UFO mass over ~ 22.5 kyr. Fortunately, it is the total energy budget of the hot shocked wind bubble and not its minuscule mass that determines the strength of the bubble's impact on the ambient medium (the mass of the UFO is so small compared to the host galaxy that it does not even enter in the analytic theory; King 2010). Therefore we rescale the properties of the UFO particles, keeping the hot bubble's energy at a desirable value but increasing the outflow's mass, to be able to model the thermalized UFO hydrodynamically and with a reasonable numerical resolution. In particular, the UFO thermalized in the reverse shock is introduced in the initial condition as a hot spherical bubble of radius $R_{\rm bub} = 0.3$ kpc centred on the sink particle. We have tested different bubble masses and find that, qualitatively, the main conclusions of our paper remain unchanged.

The initial gas density and temperature are assumed constant throughout the bubble, as expected (Faucher-Giguère & Quataert 2012). The temperature and mass of the bubble are determined based upon the desired energy ratio between the hot bubble and the ambient gas component:

$$E_{\rm r} = \frac{E_{\rm H}}{E_{\rm a}} = \frac{M_{\rm H} c_{\rm s}^2}{M_{\rm a}\sigma^2} \qquad (4)$$

where $E_{\rm H}$ and $E_{\rm a}$ are the energy in the hot bubble and the ambient gas, respectively, $M_{\rm H}$ and $M_{\rm a}$ are the total mass in the hot and cold component, respectively, $c_{\rm s}$ is the sound speed in the hot bubble and $\sigma \simeq 212$km s^{-1} is the velocity dispersion. All simulations presented in this paper use $c_{\rm s} \simeq 3000$ km s^{-1} and $E_{\rm r} = 5$; the main conclusions of our paper are independent of $E_{\rm r}$ as long as $E_{\rm r} \gg 1$, as expected for AGN-inflated feedback bubbles (King 2010). The left-most panels in Fig. 2 show the initial density and temperature structure of the system.

As well as the runs with a turbulent medium, we have a control simulation that has not been seeded with turbulence to contrast the outcomes. The radial gas distribution of the control run follows the same profile as the turbulent shell *before* relaxation, so that the gas is homogeneous, but has a mass equal to that of the turbulent shell *after* relaxation. The initial radially binned gas distribution is hence identical for the homogeneous and turbulent runs save for a slight evolution during relaxation of the latter runs as described above (compare the dashed red and blue curves in Fig. 3).

It should also be noted that the control run has a low initial temperature $T \simeq 10^5$ K, which is subvirial in order to ensure that the gas remains homogeneous during the simulation, which is the regime we wish to study here. Further, since there is no imposed turbulent velocity field that would develop into the turbulent multiphase ISM, there is no need to relax this initial condition before applying the hot bubble. For this reason, the gas has a zero initial velocity in the homogeneous control run, unlike the turbulent run. This difference in initial conditions has a very minor effect on the final outcome of the simulations because the radial velocity

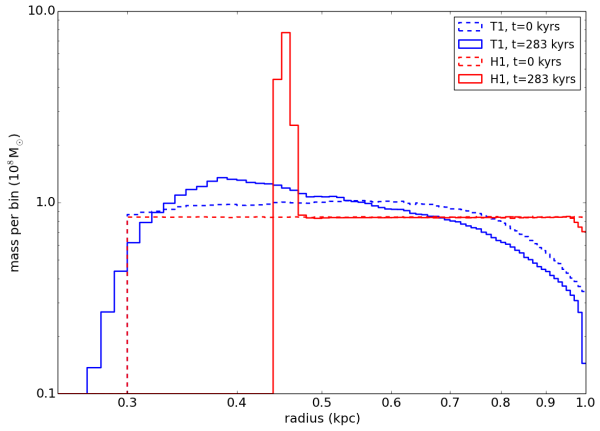

Figure 3. Histogram of the gas mass in radial bins. The blue and red lines are for the turbulent clumpy (T1) and homogeneous (H1) gas distributions, respectively. The dashed and solid lines correspond to times $t = 0$ kyr and $t \simeq 283$ kyr, respectively. Note how little the clumpy distribution evolves: if anything, gas continues to accumulate in the innermost region, whereas it is completely blown away in the H1 run.

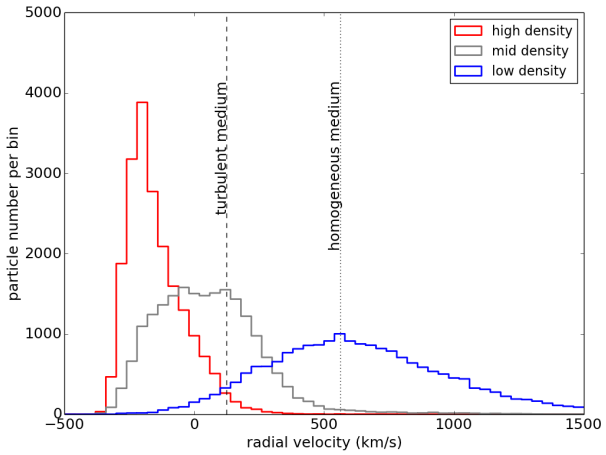

Figure 4. Histogram of the radial velocity distributions $t = 70.8$ kyr for SPH particles that belong to one of the three representative density groups, i.e., the highest 10%, around the logarithmic mean and the lowest 10% of SPH particle densities, as labelled in the inset. Particles selected were within $R \leqslant 0.35$ kpc at $t = 0$ kyr, as explained in the text

gained by the gas in the homogeneous run is much larger than the difference in the initial velocities in the two runs.

In what follows we refer to the simulations as the turbulent (T1) and control (homogeneous, H1) runs, respectively. In order to study the direct impact of the hot bubble on the ambient gas and/or to avoid confusion due to the dense gas phase shielding lower density gas behind it (at larger radii), a number of figures only include the SPH particles that were within $0.3 \leqslant R \leqslant 0.35$ kpc at $t = 0$ kyr. Behaviour of gas initially at larger radii will nevertheless be discussed in some of the figures below.

3 FEEDBACK ON TURBULENT VERSUS HOMOGENEOUS MEDIUM

Fig. 1 shows density (top) and temperature (bottom) slices at time $t = 0$ (left) and $t \simeq 283$ kyr (right) for the homogeneous density run, H1. Fig. 2 shows the same quantities at four different times for the turbulent initial condition simulation T1. The times of the first and the last snapshots are the same as those for Fig. 1.

It is immediately obvious that the homogeneous ambient density case, H1, produces a "boring" spherically symmetric, dense, shell that is expanding under the pressure of the hot bubble in the middle. The bubble also remains spherically symmetric.[3] Importantly, the bubble drives *all* of the ambient gas encountered outward at a high velocity.

This is in stark contrast to the turbulent run as can be seen in Fig. 2. The expansion of the hot bubble into the ambient phase occurs along the paths of least resistance. The low-density ambient phase is swept up and pushed out, while the high-density gas suffers a much smaller positive radial acceleration and little (if any) gain in temperature. Some compression and ablation of the cold dense medium does occur, but most of it survives the bubble's passage intact.

Fig. 3 highlights the differences in the results of simulation H1 and T1 in a more compact way by presenting the distribution of gas in radial bins. The blue and red dashed curves show the initial ambient gas mass within concentric spherical shells of 10 pc width for the turbulent and the homogeneous (control) runs, respectively. The solid curves of the same colour show how these gas distributions evolve by time $t \simeq 283$ kyr. Note that the bubble swept up *all* of the ambient gas within a radius of ~ 0.45 kpc into a dense shell in the control run, but is obviously having great difficulties in removing the gas in the turbulent simulation. The density of the gas in the inner regions actually increases in the latter simulation as some of the cold dense gas falls in while the hot bubble fizzles out through the pores in the ambient gas.

These results illustrate clearly the main thesis of our paper: *the impact of an UFO on the inhomogeneous multiphase medium is much less efficient than expected based on spherically symmetric modelling.*

4 DYNAMICS OF CLUMPY GAS

4.1 Gas dynamics as a function of its density

We shall now analyse the response of the ambient gas to the presence of the hot bubble in the turbulent simulation T1 in greater detail. This response is a strong function of the properties of the ambient gas. Fig. 4 shows the distribution of gas over radial velocity at time $t \simeq 70.8$ kyr, for three different initial density ranges (i.e. particles are grouped based upon their density at $t = 0$). To avoid confusion due to dense gas phase shielding lower density gas behind it and there-

[3] There may be small scale Vishniac (1983) instabilities developing on the surface of the bubble (Nayakshin & Zubovas 2012), but these instabilities grow slower than the shell is driven outward in this energy-conserving situation.

fore unaffected by the feedback flow yet, we include only the SPH particles that were within $0.3 \leqslant R \leqslant 0.35$ kpc at $t = 0$ kyr. The red and blue histograms show particles that originally have the highest and lowest densities whilst the grey curve shows particles at the logarithmic mean density. Each of the histograms accounts for $\sim 10\%$ of the total number of particles within $0.3 \leqslant R \leqslant 0.35$ kpc at $t = 0$ kyr. Fig. 4 demonstrates that the lowest density gas is accelerated to high radial velocities, with a mean of $\langle v_{\rm r} \rangle \simeq 661$ km s^{-1}. In contrast, the highest density gas is, on average, continuing to infall, with a mean $\langle v_{\rm r} \rangle \simeq -145$ km s^{-1}. The logarithmic mean density gas shows a variety of behaviours from an infall with velocity of a few hundred km s^{-1} to an outflow with a similar range in velocities.

Also plotted are lines indicating the mean radial velocity of all of the gas originally in the $0.3 \leqslant R \leqslant 0.35$ kpc region in the turbulent simulation ($\langle v_{\rm r} \rangle \simeq 125$ kms^{-1}) and in the homogeneous control run. In the later case the gas is accelerated to high velocities on average ($\langle v_{\rm r} \rangle \simeq 563$ kms^{-1}), in a single spherical shell of swept up material whilst in the turbulent simulation the hot bubble can escape through the porous medium and so much of the material does not get accelerated outwards. For the turbulent simulation, not only does the outflow fail to clear out the high-density material, a large fraction of the low-density material is also left behind due to shielding by high-density material in front of it.

4.2 The column density perspective

Whilst Fig. 4 highlights that gas of different densities is affected by the outflow differently, it also shows that there is an overlap in their radial velocities: some low-density gas is infalling whilst some high-density gas is outflowing. This behaviour may partially be due to gas at larger radii being shielded from the feedback by dense gas at smaller radii. To remove this self-shielding effect in our analysis somewhat, we consider the column density of the gas calculated as the integral

$$\Sigma = \int_0^R dr \rho(r, \Theta, \phi) \ , \tag{5}$$

along the lines of sight (defined by the spherical coordinate angles Θ and ϕ) from the centre of the galaxy.

Fig. 5 shows the column density map as a function of the position on the sky as viewed from $R = 0$. Only ambient gas located inside $R \leqslant 0.35$ kpc at $t = 70.8$ kyr is taken into account in this analysis. The column density of the ambient gas, Σ, calculated in this way, varies by a factor of about 1000 in Fig. 5.

Fig. 5 also presents gas radial velocity information by showing contour lines for zero velocity gas (red). Material inside of these contours has a negative radial velocity at this time. We can see that it is the gas with the highest Σ that remains infalling, whilst gas with a low Σ generally has positive radial velocities.

The complex nature of gas dynamics in the turbulent simulation makes defining and analysing the exact dynamics of gas difficult if not impossible since gas density changes during the simulation. Some of the gas may even switch phases when it cools or heats up. However we can carry out an approximate analysis by considering the momentum equation for a clump,

$$\frac{d}{dt}\left(m_{cl} v_{cl}\right) = \pi r_{cl}^2 P_{\rm ram} - \frac{G m_{cl} M(R)}{R^2} \tag{6}$$

where r_{cl}, m_{cl} and v_{cl} are the clump's radius, mass and radial velocity, respectively, $P_{\rm ram}$ is the hot bubble's ram pressure acting on the clump, R is the radial position of the clump and $M(R)$ is the mass of material within R. Making the assumption that m_{cl} and r_{cl} remain approximately constant we can divide through by m_{cl}, and re-write equation 6 as

$$a_{cl} = \frac{P_{\rm ram}}{\Sigma_{cl}} - a_{grav} \tag{7}$$

where a_{cl} and a_{grav} are the clump's acceleration and gravitational acceleration, respectively, and $\Sigma_{cl} = m_{cl}/\pi r_{cl}^2$ is the column density of the clump. The ram pressure of the hot gas cannot be predicted exactly by the analytical model, but we assume that hot gas streams out of its initial spherical configuration at approximately the sound speed of the hot gas through numerous "holes" in the cold ambient gas distribution. This argument suggest that by the order of magnitude $P_{\rm ram}$ should be comparable to the initial isotropic pressure of the hot gas, P.

When $\Sigma_{cl} << P/a_{grav}$, the driving force of the bubble dominates over gravity and we can neglect the a_{grav} term in equation 7, integrating then gives an estimate for a clumps velocity at time t as

$$v(t) = \frac{P_{\rm ram}}{\Sigma_{cl}} t + v(0). \tag{8}$$

Setting $v(t) = 0$ we can define a critical column density,

$$\Sigma_{crit}(t) = \frac{P_{\rm ram}}{|v(0)|} t \tag{9}$$

such that only material with $\Sigma > \Sigma_{\rm crit}$ should still be infalling at time t, whereas lines of sight with $\Sigma < \Sigma_{\rm crit}$ may be launched in an outflow.

Using the mean radial velocity of gas particles at $t = 0$ for v_0, we find $\Sigma_{\rm crit} \gtrsim 0.36$ g cm^{-2} at $t \sim 70.8$ kyr. Black contours in Fig. 5 show the lines of sight where $\Sigma = \Sigma_{\rm crit}$. We see that there is a close agreement between the red (zero velocity contours) and the black contour lines, suggesting that the approximate analysis based on equation 7 does have a certain merit to it. This could be expected from theoretical studies of how a single dense gas cloud is affected by a hot bubble (e.g., McKee & Cowie 1975), N14. The column density of the cloud, Σ, is roughly the product of the mean cloud density, $\rho_{\rm cl}$, and the physical size of the cloud, $r_{\rm cl}$. Therefore, a dense but physically small (small $r_{\rm cl}$) cloud may have a smallish Σ, and is accelerated to a significant radial velocity by the UFO, and hence may be completely destroyed, despite being dense. A dense and large (large $r_{\rm cl}$ and Σ) cloud, on the other hand, may both withstand the onslaught from the hot bubble and also continue to infall.

There are a few caveats to this approach for comparing Σ and expected radial velocity. The high Σ regions shown in the plot can only be considered an estimate for the high-density material as they are calculated based upon the entire contribution of material along a particular line of site out to $R \leqslant 0.35$ kpc. This leads to potentially over(under)estimating Σ if the clump extends to radii that are less (greater) than 0.35 kpc. Further we use an average value for v_0 and assume that the column density of the

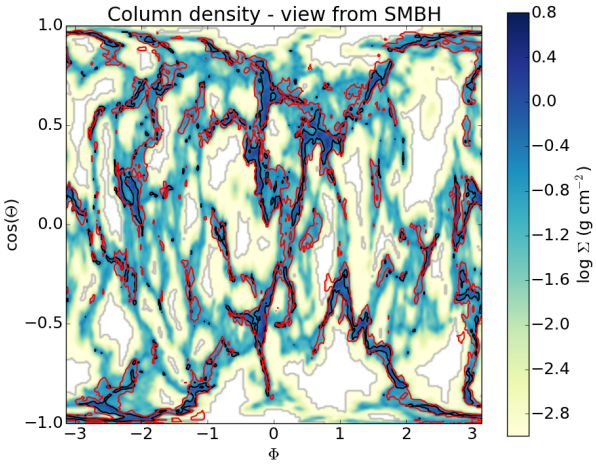

Figure 5. Column density of ambient gas at $R \leqslant 0.35$ kpc at $t = 70.8$ kyr, as viewed from the position of the sink particle. Also plotted are contour lines for zero velocity gas (red) and gas with $\Sigma_{\rm crit} = 0.36$ g cm^{-2}, which is analytically predicted to have zero velocity at this time. Note that the two contour lines coincide over most of the plot.

clump remains approximately constant over the time period considered. Therefore the estimate here should only be considered as a rough illustration of the interaction of the high-density clumps with the expanding bubble and not an exact solution, which would require a far more detailed analysis than is necessary for the purposes of this paper.

4.3 Time evolution of the outflow

So far we have only shown properties of the system at specific moments in time, however, a consideration of the time evolution of the system is also important. Fig. 6 shows the time evolution of the change in mean radial position, $\Delta R = \overline{R}(t) - \overline{R}(0)$ (top) and change in mean radial velocity $\Delta v = \overline{v}(t) - \overline{v}(0)$ (bottom) for ambient gas particles initially at $R \leqslant 0.35$ (these particles are chosen to avoid other complicating factors such as shielding of low density gas). The solid red and blue lines on these figures are taken from the homogenous simulation H1 and turbulent simulation T1, respectively. Also shown on each of the panels in Fig. 6 is three blue lines calculated from the data of the turbulent simulation T1, showing the change in mean radial position (top) and mean radial velocity (bottom) for low (dotted), intermediate (dashed) and high (dot-dashed) density gas. We apply fixed density thresholds set at the values used in Fig. 4 earlier, however, unlike in Fig. 4, where particles are grouped based upon their original density, here the particles are grouped based upon their density at time t. Both the change in mean radial position and mean radial velocity plots demonstrate again that the low-density gas is affected by the hot bubble much stronger than the high density gas. Both panels of Fig. 6 show a certain reduction in the difference between the three density groups as time goes on which is however due to (a) mixing between the two phases with time, and (b) the fact that the bubble energy is not replenished in our simulation.

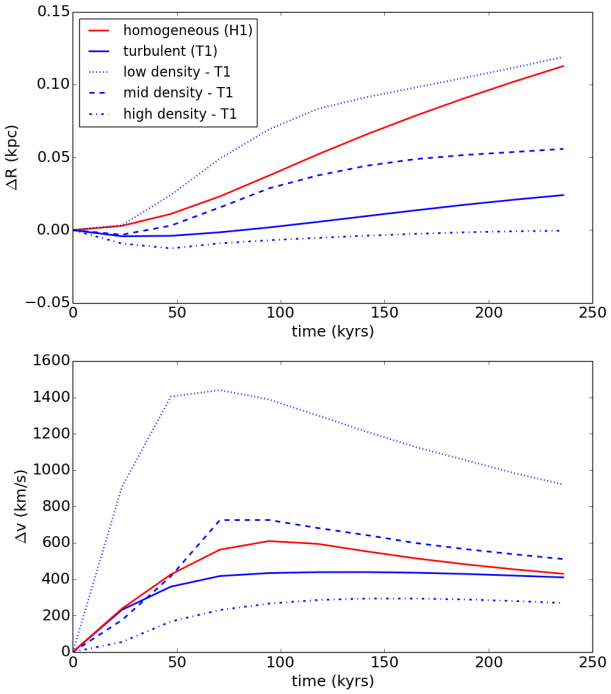

Figure 6. Time evolution of the change in mean radial position (top) and change in mean radial velocity (bottom) of gas in the homogeneous (H1, red) and turbulent (T1, blue) runs. In the latter case the gas is further divided into low (dotted), intermediate (dashed) and high (dash-dot) density material.

4.4 Decoupling of energy and mass flow

In the homogeneous control simulation H1, both mass and energy are flowing outward as the bubble expands. The situation is bound to be far more interesting in the case of the turbulent simulation T1, since we saw in Section 4.1 that there is both an inflow and an outflow at the same time. Furthermore, since the different phases have widely different radial velocities and temperatures, the overall direction of the flow of mass and energy is not obvious.

To analyse these flows we define the rate of mass and energy flows in a given radial bin of width Δr_{bin}, respectively, as

$$\dot{M} = \sum \frac{m_{sph} v_r}{\Delta r_{bin}} \tag{10}$$

$$\dot{E} = \sum \left[\frac{1}{2} v^2 + \frac{3}{2} \frac{k_B T}{\mu m_p} \right] \frac{m_{sph} v_r}{\Delta r_{bin}} \, . \tag{11}$$

The SPH particles in this sum are selected based on criteria placing them in one or the other phase or group (see below). In a steady state spherically symmetric flow, these definitions would include all of the SPH particles in a bin, and would then give the total mass and energy flux rate as a function of position in the flow.

In the homogeneous control run, the energy and mass flows are dominated by outflowing material but only within the radius of the swept up shell, beyond this there is no outward $\dot{E}$ and $\dot{M}$, while the inward values are negligibly small.

Fig. 7 shows $\dot{E}$ (top) and $\dot{M}$ (bottom) for in-flowing

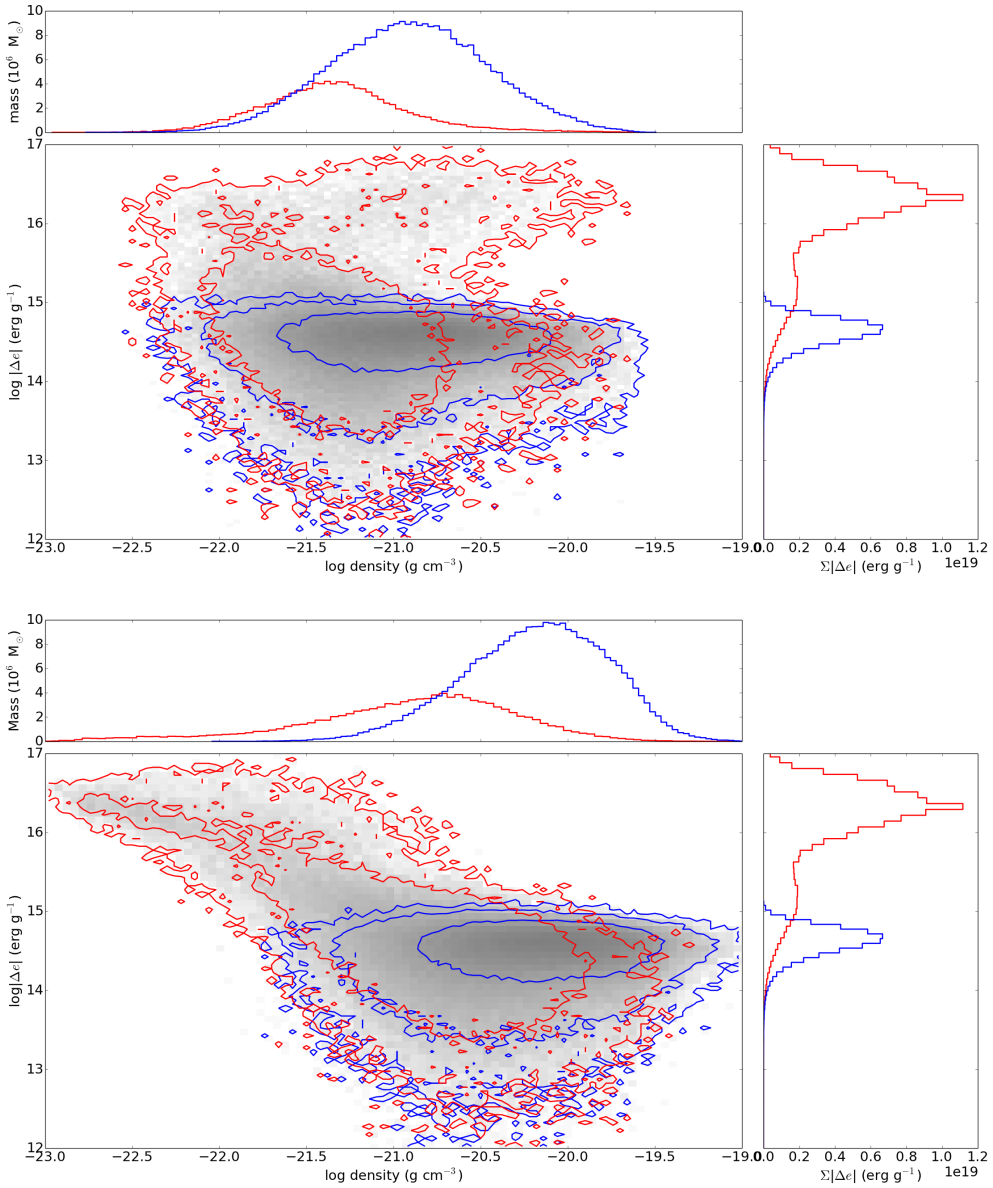

Figure 8. Particle distribution plot of absolute change in specific energy between $t = 0$ and 189 kyr (Δe) against original gas density (top) and current gas density (bottom). Contours indicate gas that has lost energy (blue) or gained energy (red). The density axis have been collapsed into one-dimensional mass histograms above each panel whilst the energy axis has been collapsed into one-dimensional histograms weighted by Δe to the right of each panel.

($v_r \leqslant -\sigma/2$, blue) and outflowing ($v_r \geqslant \sigma/2$, red) material in the turbulent simulation T1, binned radially at $t = 283$ kyr. Both panels show that, unlike the spherically symmetric situation (simulation H1), there are outflows and inflows of mass and energy for all radii in the clumpy simulation T1. Interestingly, the energy flow is dominated by the material streaming outward, which we identify with the hot low-density gas based on our earlier analysis, whereas the mass flow is mainly inward and is dominated by the high density gas. This shows that *energy and mass flows separate from one another in turbulent flows*. Unlike the spherically symmetric homogeneous case, energy does not necessarily flows where most of the mass does.

To analyse this energy-mass decoupling further, we define the absolute change in specific energy of SPH particles as

$$|\Delta e| = \left| \frac{1}{2}\left(v^2 - v_0^2\right) + \frac{3}{2}\frac{k_B}{\mu m_\mathrm{p}}\left(T - T_0\right) + G\frac{M_a}{a}\ln\left(\frac{R}{R_0}\right) \right| \tag{12}$$

where the terms on the right hand side are the change in specific kinetic, internal and gravitational potential energy, respectively (note we only include the gravity due to the underlying potential). v, T and R are the velocity, temperature and radial positions of each particle, respectively, with the subscript 0 indicating the initial value of each of these parameters.

Fig. 8 shows the absolute change in SPH particle specific energy ($|\Delta e|$) between $t = 0$ and 189 kyr versus the gas density at the initial time (the top panel), and, alternatively, versus the gas density at $t = 189$ kyr (the bottom

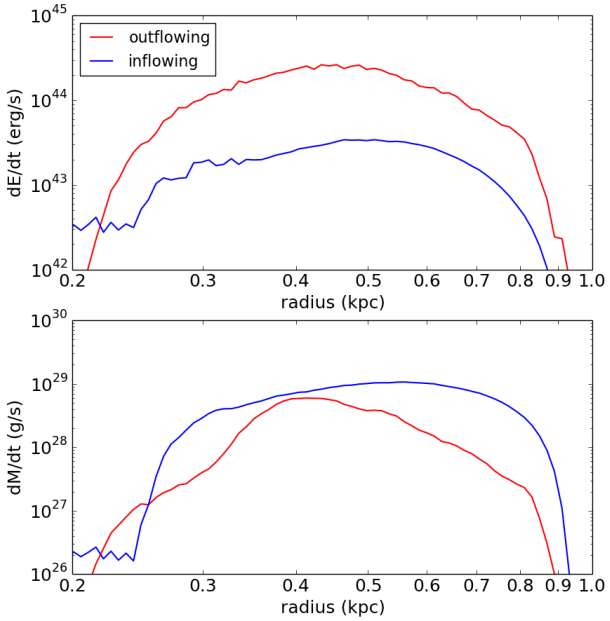

Figure 7. Radial flows of energy, $\dot{E}$ (top panel), and mass, $\dot{(M)}$ (bottom panel), for gas that is either in-flowing (blue) or outflowing (red) at time $t = 283$ kyr in the simulation T1.

panel). Contours indicate gas that has lost energy (blue) or gained energy (red). The density axis has been collapsed into one-dimensional mass histograms, located at the top of each plot, whilst the energy axis has been collapsed into one-dimensional histograms weighted by Δe, located to the right of each plot. As before (e.g., Fig. 4), only particles within $R = 0.35$ kpc at $t = 0$ are selected for this analysis to minimize complications due to gas self-shielding.

Since gas in simulation T1 is initially infalling due to our initial conditions, so that radial velocity $v_r < 0$, particles that loose specific energy (blue colour in fig. 8) correspond to particles that are, in general, only moderately affected by the hot bubble. The radial velocity of such particles is either still negative but less so than initially or has a small positive value. On the other hand, particles with a positive energy change (red), as a rule, are particles that are now outflowing with a larger positive v_r.

Focusing on the 1D mass distributions, above the corresponding panels, we observe from the figure that most of the mass is in the blue gas that is on average denser than the red (outflowing) gas. At the same time, 1D energy distributions to the right of each panel, show that most energy is in the red SPH particles, so that, consistent with Fig. 7, energy is mainly in the low-density outflowing particles. The low-density tail of the distribution of the red particles in the bottom panel shows that the energy gained by the outflowing particles may be about two orders of magnitude higher than the energy change of the blue dense particles.

Further, comparing the top and the bottom panels, we see that the low-density outflowing gas tail in the bottom panel had on average higher density at time $t = 0$. This gas is initially moderately dense but has been ablated from the surface of the clouds and launched in the outflow by the hot bubble. The SPH particles in the blue part of the distribution had their density increased by a factor of several. The hot bubble thus compresses most of the dense gas by a factor of at least a few. This is consistent with earlier results of Nayakshin & Zubovas (2012) (see also Silk & Norman (2009)) showing that AGN outflows may in fact trigger star formation in dense cold gas by compressing it to very high densities.

5 DISCUSSION

5.1 Feedback on a homogeneous versus a multiphase ISM

We have studied the impact of a thermalized UFO launched by a rapidly accreting SMBH (modelled as a hot bubble) on the ambient gas of the host galaxy in two contrasting limits. In the first, the ambient gas is initially homogeneous and spherically symmetric, whereas in the second limit it is highly inhomogeneous due to an initially imposed turbulent velocity field. In broad agreement with previous work (W12, W13, N14 and ZN14), we find marked differences in the outcome of this interaction.

We find that the homogeneous spherically symmetric ambient gas is driven outward by the hot bubble much in the same way as described by the energy-conserving analytical models of AGN feedback (e.g., King 2003, 2005, 2010; Zubovas & King 2012a; Faucher-Giguère & Quataert 2012). In such models the ambient gas is only driven away if the feedback is sufficiently strong and the weight of the medium sufficiently small. In a stark contrast to this, the turbulent clumpy ISM cannot easily be described in a 1D language. Because of a large density contrast between the different phases in the ISM, there is simultaneously inflowing and outflowing gas streaming throughout the host galaxy.

The cold dense medium is affected by the UFO significantly less than analytic models, quoted above, assume because the medium is overtaken by the UFO rather than being pushed in front of it. We find that some high-density clumps continue to move inward while the hot bubble fizzles out through low-density 'pores' and accelerates the low-density phase of the ISM to high outward velocities. Analysis of this behaviour shows that the cold dense phase gets an initial kick from the pressure of the bubble before it is overtaken, after which the driving force acting on the clump diminishes.

Another important result found here is a divergence in the directions of where most of the mass and energy flow in a turbulent ISM. While most of the mass is flowing inward, carried by the cold dense clouds which continue to infall despite AGN feedback, most of the UFO energy manages to percolate through the ambient ISM and flow outward through the bulge.

5.2 Pertinence to the $M - \sigma$ relation

Overall, our results suggest that the establishment of the $M - \sigma$ relation is much more complicated a process than in spherically symmetric models (e.g., Silk & Rees 1998; Fabian 1999; King 2003). In such models, the $M - \sigma$ mass divides two very different regimes. SMBHs below the $M - \sigma$ mass are unable to drive the gas outward beyond a small radius (tens

to a few hundred pc, depending on the BH mass and the host velocity dispersion). It is only once the SMBH exceeds the $M-\sigma$ mass the outflow is able to overcome the weight of the ambient gas in the galaxy and clear *all of the host* of its gas. This paints an all or nothing picture of AGN feedback (above or below the $M-\sigma$ mass, respectively).

The picture of AGN feedback changes radically if the ISM in the host is multiphase. There is no longer the two different regimes with a sharp boundary, the $M-\sigma$ mass, between them: at any SMBH mass there may be an inflow and an outflow of gas at the same location in the host and at the same time.

This must dilute the meaning of the $M-\sigma$ mass, because, on the one hand, "underweight" SMBHs, i.e., those below the $M-\sigma$ mass, do have an influence on the host galaxy even on large scales. Since the hot gas propagates outward by finding and following the paths of least resistance, the low-density phase at all radii in the host is vulnerable to AGN feedback. On the other hand, the high-density medium is more resilient to SMBH feedback than could be thought based on spherically symmetric models because the medium is over-taken by the UFO rather than being pushed in front of it. N14 and ZN14 proposed that this unexpected resilience of the host gas to AGN feedback explains how SMBH manage to grow to the momentum-limited M_σ masses (King 2003) rather than the energy-limited ($\sim$ 100 times lower) masses.

One speculation arising from these results is that a tight $M-\sigma$ relation could actually never be established in an ensemble of *isolated* galaxies, and that mergers of galaxies are crucial to the emergence of the observed relations. On the basis of results presented here and in ZN14, we argue that there are simply too many factors determining the SMBH interaction with the host galaxy (the ISM structure, angular momentum of the gas, etc.), and that therefore one should expect a very significant spread in any SMBH-host relation based on *a single episode* of the galaxy and the SMBH growth. It is likely that averaging occurring during mergers of galaxies (the central limit theorem applied to mergers, see e.g., Jahnke & Macciò 2011) largely erases this significant spread, leading to a tight $M-\sigma$ relation at low redshift. This view is consistent with the fact that the observed SMBH-host scaling relations are only tight for classical bulges and ellipticals, that the scatter in such relations decreases towards higher masses, and that SMBH–host relations have larger scatter at large redshifts (Kormendy & Ho 2013).

5.3 Induced star formation and stellar feedback

Comparing the top and the bottom panels of Fig. 8, or the blue curves in the horizontal histograms above these panels, we see that the mean density of the dense material increases with time in the simulation T1. Because of this density increase, a small number of star particles are formed in our simulation, in a broad agreement with the earlier suggestions of AGN-induced star formation (Nayakshin & Zubovas 2012) (see also Silk & Norman (2009)). Such *positive* AGN feedback is likely unresolved in cosmological simulations.

5.4 Comparison with other work

Out of previous literature, our work is most similar in spirit to W12 and W13, with a number of similar conclusions. One difference, however, is that W13 finds that the dense clouds are heated strongly and accelerated outwards as a result of the feedback (albeit slower than the hot phase). In our work inflows occur *despite* the feedback.

The response of the cold phase to the UFO is strongly dependent on the initial conditions of the phase and the physics included in the simulation. In W13, radiative cooling below a temperature of 10^4 K is turned off, which clearly limits the highest densities that could be reached by the cold phase under the external compression by the hot medium. In our simulations, self-gravity of the clouds is an important factor in ensuring the integrity of the clouds when they are hit by the UFO. W12 and W13, on the other hand, do not include self-gravity of the gas and the initial densities of the clouds appear to be comparable to the tidal densities at the clouds' locations. In our opinion, cold clouds in W12 and W13 are both susceptible and defenceless to shear from the gravitational potential and hydrodynamic forces by the UFO.

In any event, we believe that neither our study nor the previous work gives complete and *quantitatively* definitive answers on the interaction of the UFO and a clumpy turbulent medium of the host galaxy. Future simulations should focus on modelling the physical properties of the ISM with a greater realism, in particular including star formation and its feedback (which we did not include here).

5.5 Implications for cosmological simulations

Cosmological simulations (e.g., Di Matteo et al. 2008; Schaye et al. 2010; Dubois et al. 2012) often invoke AGN feedback in order to reproduce observed relationships such as the galaxy luminosity function. In this sense AGN provide a source of negative feedback and therefore the mechanism of the subgrid prescription employed acts to inhibit star formation and eject gas from a galaxy. This is normally achieved through heating or "kicking" gas local to the black hole. Such simulations, which by necessity, balance on the edge of what is numerically achievable, are unable to resolve the multiphase ISM. It is likely that any feedback would be acting on a single phase medium. The heterogeneous effects that feedback has on the different phases of a multiphase ISM illustrated in our simulations may then be lost due to numerical limitations.

The extent to which this poses a problem depends upon the exact nature of the multiphase ISM (Wagner et al. 2012) and upon the problem that one wishes to investigate with the cosmological simulations. With regards to meeting large-scale observational trends, such as the galaxy luminosity function or $M-\sigma$ relation, the subgrid models employed by cosmological simulations may be sufficient. However, as shown in this paper, the exact nature of the ISM does impact how AGN feedback couples with the ambient gas in a galaxy. In our simulations, the cold dense phase is mainly affected by the ram pressure (momentum) of the UFO, whereas the low-density phase bears the brunt of the UFO's energy content. In contrast, widely used AGN feedback models (e.g., Di Matteo et al. 2008; Dubois et al. 2012) tend to neglect the

physical state of the gas and instead focus on the proximity of the gas to the SMBH. Even though cosmological simulations are currently unable to resolve the ISM, there may still exist material with a range of physical properties close to black hole. It is therefore likely that the robustness of cosmological simulations could be improved by a set of prescriptions that incorporate the physics highlighted by our simulations. Similarly, semi-analytical models (e.g., Bower et al. 2006) may benefit from including an energy-leaking prescription for the hot bubble (see ZN14).

6 CONCLUSION

We have studied the impact of a thermalized UFO (modelled as a hot bubble) launched by a rapidly accreting SMBH on the ambient gas of the host galaxy in two contrasting limits. In the first, the ambient gas is initially homogeneous and spherically symmetric, whereas in the second limit it is highly inhomogeneous due to an initially imposed turbulent velocity field. In a broad agreement with previous work (W12, W13, N14 and ZN14), we find marked differences in the outcome of this interaction. In particular, most of the UFO's energy escapes via low-density channels in the clumpy ISM, which drastically reduces the impact of the UFO on the dense cold phase that contains most of the ambient gas in the host galaxy. We conclude that the state of the ISM in a galaxy is just as important as the AGN feedback model invoked, in determining how AGN feedback interacts with the ambient medium.

Given the complexity of these processes, the meaning of the $M-\sigma$ mass becomes much less defined than in spherically symmetric analytic models (e.g., Silk & Rees 1998; Fabian 1999; King 2003). In the latter, SMBH below the $M-\sigma$ mass are unable to 'clear' their host galaxies and hence continue to grow, whereas SMBH above this mass terminate their and their host's growth by expelling all the gas. In a turbulent ISM, there may be outflows – of the low density phase – at $M_{\rm bh} \ll M_\sigma$, but there could also be inflows – of the high-density phase – at $M_{\rm bh} \gg M_\sigma$. We therefore concluded in §5.2 that it is hard to see how tight SMBH-host correlations could occur in an ensemble of *isolated* galaxies, and that mergers of galaxies must be crucial to the emergence of the observed relations. The interesting question arising from this, then, is to what extent can the observed correlations be attributed to AGN feedback physics and to what extent be due to the central limit theorem (Jahnke & Macciò 2011).

ACKNOWLEDGEMENTS

We acknowledge an STFC grant and an STFC research studentship support. We thank Hossam Aly, Alex Dunhill and Kastytis Zubovas for useful discussions, and Justin Read for the use of SPHS. This research used the ALICE High Performance Computing Facility at the University of Leicester and the DiRAC Complexity system, operated by the University of Leicester IT Services, which forms part of the STFC DiRAC HPC Facility (www.dirac.ac.uk). This equipment is funded by BIS National E-Infrastructure capital grant ST/K000373/1 and STFC DiRAC Operations grant ST/K0003259/1. DiRAC is part of the UK National E-Infrastructure. Figs. 1 and 2 were produced using SPLASH (Price 2007).

REFERENCES

Bate M. R., 2009, MNRAS, 392, 590
Bate M. R., Bonnell I. A., Bromm V., 2003, MNRAS, 339, 577
Binney J., Tremaine S., 2008, Galactic Dynamics: Second Edition, Princeton University Press
Bourne M. A., Nayakshin S., 2013, MNRAS, 436, 2346
Bower R. G., Benson A. J., Malbon R., et al., 2006, MNRAS, 370, 645
Dehnen W., Aly H., 2012, MNRAS, 425, 1068
Di Matteo T., Colberg J., Springel V., Hernquist L., Sijacki D., 2008, ApJ, 676, 33
Dubinski J., Narayan R., Phillips T. G., 1995, ApJ, 448, 226
Dubois Y., Devriendt J., Slyz A., Teyssier R., 2012, MNRAS, 420, 2662
Fabian A. C., 1999, MNRAS, 308, L39
Faucher-Giguère C.-A., Quataert E., 2012, MNRAS, 425, 605
Ferrarese L., Merritt D., 2000, ApJL, 539, L9
Gebhardt K., Bender R., Bower G., et al., 2000, ApJL, 539, L13
Harper-Clark E., Murray N., 2009, ApJ, 693, 1696
Hobbs A., Nayakshin S., Power C., King A., 2011, MNRAS, 413, 2633
Hobbs A., Read J., Power C., Cole D., 2013, MNRAS, 434, 1849
Jahnke K., Macciò A. V., 2011, ApJ, 734, 92
King A., 2003, ApJL, 596, L27
King A., 2005, ApJL, 635, L121
King A. R., 2010, MNRAS, 402, 1516
King A. R., Pounds K. A., 2003, MNRAS, 345, 657
Kormendy J., Ho L. C., 2013, ARA&A, 51, 511
Mashchenko S., Wadsley J., Couchman H. M. P., 2008, Science, 319, 174
McKee C. F., Cowie L. L., 1975, ApJ, 195, 715
McKee C. F., Ostriker J. P., 1977, ApJ, 218, 148
Nayakshin S., 2014, MNRAS, 437, 2404
Nayakshin S., Zubovas K., 2012, MNRAS, 427, 372
Pounds K. A., Reeves J. N., King A. R., Page K. L., O'Brien P. T., Turner M. J. L., 2003, MNRAS, 345, 705
Pounds K. A., Vaughan S., 2011, MNRAS, 413, 1251
Price D. J., 2007, PASA, 24, 159
Read J. I., Hayfield T., 2012, MNRAS, 422, 3037
Read J. I., Hayfield T., Agertz O., 2010, MNRAS, 405, 1513
Rogers H., Pittard J. M., 2013, MNRAS, 431, 1337
Sazonov S. Y., Ostriker J. P., Ciotti L., Sunyaev R. A., 2005, MNRAS, 358, 168
Schaye J., Dalla Vecchia C., Booth C. M., et al., 2010, MNRAS, 402, 1536
Silk J., Norman C., 2009, ApJ, 700, 262
Silk J., Rees M. J., 1998, A&A, 331, L1
Springel V., 2005, MNRAS, 364, 1105
Tombesi F., Cappi M., Reeves J. N., et al., 2010a, A&A, 521, A57+

Tombesi F., Sambruna R. M., Reeves J. N., et al., 2010b, ApJ, 719, 700
Tremaine S., Gebhardt K., Bender R., et al., 2002, ApJ, 574, 740
Vishniac E. T., 1983, ApJ, 274, 152
Wagner A. Y., Bicknell G. V., Umemura M., 2012, ApJ, 757, 136
Wagner A. Y., Umemura M., Bicknell G. V., 2013, ApJL, 763, L18
Wendland H., 1995, Advances in computational Mathematics, 4, 1, 389
Whitworth A. P., 1998, MNRAS, 296, 442
Zubovas K., King A., 2012a, ApJL, 745, L34
Zubovas K., King A. R., 2012b, MNRAS, 426, 2751
Zubovas K., Nayakshin S., 2014, MNRAS, 440, 2625